Adaptive rewiring of purine metabolism promotes treatment resistance in H3K27M-mutant diffuse midline glioma

Erik R. Peterson
University of Michigan
Peter Sajjakulnukit
University of Michigan
Andrew J. Scott
University of Michigan
Caleb Heaslip
Massachusetts College of Pharmacy and Health Sciences
Anthony Andren
University of Michigan
Kari Wilder-Romans
University of Michigan
Weihua Zhou
University of Michigan
Sravya Palavalasa
University of Michigan
Navyateja Korimerla
University of Michigan
Angelica Lin
University of Michigan
Alexandra Obrien
University of Michigan
Ayesha Kothari
University of Michigan
Zitong Zhao
University of Michigan
Li Zhang
University of Michigan
Meredith A. Morgan
University of Michigan
Sriram Venneti

University of Michigan
Carl Koschmann
University of Michigan
Nada Jabado
McGill University
Costas A. Lyssiotis
University of Michigan
Maria G. Castro
University of Michigan
Daniel R. Wahl (dwahl@med.umich.edu)
University of Michigan

Research Article

Keywords: Diffuse midline glioma, H3K27M, Radiation therapy resistance, purine metabolism

Posted Date: September 11th, 2023

DOI: https://doi.org/10.21203/rs.3.rs-3317816/v1

Abstract

Background: Diffuse midline gliomas (DMG), including diffuse intrinsic pontine gliomas (DIPGs), are a fatal form of brain cancer. These tumors often carry a driver mutation on histone H3 converting lysine 27 to methionine (H3K27M). DMG-H3K27M are characterized by altered metabolism and resistance to standard of care radiation (RT), but how the H3K27M mediates the metabolic response to radiation and consequent treatment resistance is uncertain.

Methods: We performed metabolomics on irradiated and untreated H3K27M isogenic DMG cell lines and observed an H3K27M-specific enrichment for purine synthesis pathways. We profiled the expression of purine synthesis enzymes in publicly available patient data and in our models, quantified purine synthetic flux using stable isotope tracing, and characterized the *in vitro* and *in vivo* response to *de novo* and salvage purine synthesis inhibition in combination with RT.

Results: DMG-H3K27M cells activate purine metabolism in an H3K27M-specific fashion. In the absence of genotoxic treatment, H3K27M-expressing cells have higher relative activity of *de novo*synthesis and lower activity of purine salvage due to decreased expression of the purine salvage enzymes. Inhibition of *de novo* synthesis radiosensitized DMG-H3K27M cells *in vitro* and *in vivo.* Irradiated H3K27M cells adaptively upregulate purine salvage enzyme expression and pathway activity. Silencing the rate limiting enzyme in purine salvage, hypoxanthine guanine phosphoribosyl transferase (HGPRT) when combined with radiation markedly suppressed DMG-H3K27M tumor growth *in vivo.*

Conclusions: H3K27M expressing cells rely on *de novo* purine synthesis but adaptively upregulate purine salvage in response to RT. Inhibiting purine salvage may help overcome treatment resistance in DMG-H3K27M tumors.

Background

Diffuse midline gliomas (DMG) are pediatric high-grade gliomas that arise in midline structures of the brain including the thalamus, cerebellum, and pons(1–3). In 2016, the World Health Organization described a subtype of DMG that carries a driver missense mutation in the tail domain of Histone H3 that converts the 27th residue from lysine (K) to methionine (M), termed H3K27M(1, 4). Patients with DMG-H3K27M carry a dire prognosis with over 90% dying within 2 years of diagnosis(2). Treatment options are limited for patients with DMG-H3K27M tumors. Surgical resection is often unfeasible due to the eloquent function of the midline tissues in which they arise(2, 3, 5). DMG-H3K27M tumors also derive minimal benefit from systemic therapies(3, 5–7). Radiation therapy (RT) is currently the only treatment modality that provides meaningful benefit to patients and is the current standard of care(8–12). However, RT typically only extends patient survival by months, and tumors regrow within the high-dose radiation field(8, 12, 13). This suggests that DMG-H3K27M tumor cells can effectively adapt and resist RT, leading to regrowth. Simply increasing the RT dosage given is not feasible owing to limiting toxicity in normal tissue. Therefore, there is a critical need to selectively increase the sensitivity of DMG-H3K27Ms to RT.

Cellular metabolism controls RT efficacy in various tumor types, including adult brain malignancies(14–17). The H3K27M mutation causes a global shift in the epigenome, leading to large-scale gene expression changes. This is characterized by global hypomethylation of the H3K27 residue in promoter regions of H3K27M cells which is accompanied by increased activating H3K27 acetylation marks(4, 18–23). These alterations cause metabolic shifts specific for H3K27M-expressing tumors(24). Such shifts included increased dependence on methionine and pyrimidine metabolism, along with classically cancer-co-opted pathways such as glycolysis and the TCA cycle(25–27). How and whether these H3K27M-driven metabolic changes confer radiation resistance to DMGs is unknown.

The importance of the H3K27M mutation and its profound effect on metabolism suggest that this mutation may specifically confer RT resistance in DMG-H3K27M tumors. Here, we identify purine metabolism as an H3K27M-specific metabolic vulnerability that governs the RT response. Cells can synthesize the two main classes of purines (adenylates and guanylates) *de novo* from metabolic building blocks or salvage them from pre-formed nucleobases. We find that H3K27M-expressing cells preferentially utilize *de novo* guanylate synthesis during unperturbed growth, likely due to increased expression of the enzymes utilized in *de novo* synthesis and decreased expression of those used in salvage. Inhibitors of *de novo* guanylate synthesis sensitize DMG-H3K27M models to RT *in vitro* and *in vivo* but do not cure tumors. Unexpectedly, we find that H3K27M cells upregulate guanylate salvage in response to RT, which likely mediates resistance to inhibition of *de novo* purine synthesis. Knockdown of the rate limiting enzyme in guanylate salvage greatly increases RT efficacy in orthotopic H3K27M xenografts. These findings indicate that guanylate salvage inhibition may be a promising strategy to overcome RT resistance in DMG-H3K27M.

Methods

Cell Lines and Tissue Culture

Patient-derived H3K27M-isogenic (H3K27M and H3K27M-KO) cell line pairs (DIPGXIII and BT245) were generous gifts from Dr. Nada Jabado (McGill University)(20) and were cultured in Tumor Stem Media (TSM) as previously described(19).

DIPGXIII-GFP/LUC and DIPGXIII-GPF/LUC-shHPRT1 cell lines

DIPGXIII H3K27M-expressing cells were plated in TSM media containing polybrene transfection reagent and 10X ready-made lentiviral stock containing expression constructs for GFP and firefly luciferase (GFP/LUC) (Lenti-GF1-CMV-VSVG) or ready-made shHPRT1 viral vector stock (Santa Cruz Biotechnology Cat #: sc-40679-V). Cells were centrifuged and washed and expanded in 15cm plates 24hrs later. Successful transduction was confirmed by GFP expression or puromycin selection and loss of HGPRT protein.

Western Blotting

H3K27M-isogenic cells were lysed in RIPA buffer containing protease (cOmplete, Roche) and phosphatase inhibitors (phoSTOP, Roche) on ice with mechanical disruption at the start of incubation. Lysates were clarified and protein concentration was determined using BCA assay (ThermoFisher). SDS-PAGE was performed using at least 12.5ug protein on 4–20% Tris-Glycine gels. Proteins were semi-dry transferred onto nitrocellulose for 1.5hrs at 24V. Membranes were blocked in non-fat dry milk in TBST before incubation with primary antibody overnight at 4C. Membranes were washed with TBST before incubation with secondary antibody. West Pico Plus (ThermoFisher) ECL reagent and X-Ray film were used to measure expression as previously described(16). Antibodies used: H3K27M (Cell Signaling, Cat#: 74829), H3K27me3 (EMD-Millipore, Cat#: 07-449), inosine monophosphate dehydrogenase 1 (IMPDH1) (Cell Signaling, Cat#: 35914), HPRT1 (Invitrogen, Cat#: PA5-22281), beta-Actin (Santa Cruz, Cat#: sc-47778).

Histone Purification

Histone purification was performed as described previously(24). H3K27M isogenic cells (> 1.0x10^6) were suspended in 1mL hypotonic lysis buffer and lysed by mechanical shearing on a rotator at 4C. Nuclei were isolated and suspended in 0.4N H_2SO_4 overnight to precipitate histones. Samples were clarified and trichloroacetic acid was added dropwise to the histone-containing supernatant, which were mixed and incubated on ice. Histones were pelleted, washed with ice-cold acetone, and air-dried. Histones were resuspended in ddH2O. Protein content was quantified using a BCA assay.

Steady-State Metabolomics

H3K27M-isogenic cells (2-3x10^6 cells/biological replicate) were plated in 10cm dishes in TSM media and were grown to be small neurospheres (approximately 2 days in culture). Media was changed 2hrs before treatment. Cells were irradiated with 4Gy RT using a Philips RT250 (Kimtron Medical) at a dose rate of approximately 2 Gy/minute at the University of Michigan Rogel Comprehensive Cancer Center Experimental Irradiation Shared Resource (Ann Arbor, MI). Cells were incubated for 2hrs at 37°C. One plate from each group was analyzed by BCA assay quantify protein for standardization. After incubation, all cells were collected in individual 15mL conical tubes and pelleted. Supernatants were removed and metabolites were extracted with ice-cold 80% methanol on dry ice. Pellets were resuspended and incubated for on dry ice. Samples were centrifuged to clarify the metabolite extract and supernatants were transferred to new 15mL tubes. This step was repeated twice to ensure clarity. Metabolite extracts equating to roughly 1000µg of protein were transferred to 1.5mL microcentrifuge tubes before drying in a speed vacuum centrifuge or under a nitrogen blower. Liquid chromatography/mass spectrometery (LC/MS) analyses were performed as previously described(28). Agilent MassHunter Quantitative Analysis B.09.00 QqQ software was used to integrate and quantitate areas (Agilent Technologies).

Steady-State Metabolomics Data Analysis

Metabolite lists were trimmed to exclude metabolites that fell below the noise threshold. Remaining metabolite abundances were median centered. H3K27M isogenic cells were analyzed in pairs. All metabolites whose abundance changed by a Log2 FC of |0.15| following RT in either H3K27M or H3K27M-KO cells were selected and combined into a single list. These lists were ordered by the absolute value of difference in post-RT Log2FC between K27M and KO cells. The top 25 metabolites were selected for pathway enrichment analysis using MetaboAnalyst 5.0 where the top 10 most significantly represented pathways were selected(29). Statistical analyses and heatmap construction were performed using GraphPad Prism 9.0.

Stable Isotope Tracing

H3K27M isogenic cells (> 4.0x10^6 cells/replicate) were plated in 10cm dishes in TSM and grown into small neurospheres. Approximately 30min before RT, cells were pelleted and washed and replated with TSM media with stable isotope tracer molecules replacing the naturally occurring metabolites (2mM 2,8-deuterium hypoxanthine (2D-Hpx) or 4mM ^{15}N-glutamine [Cambridge Laboratories Inc, Cat#: DLM-8658 and NLM-557, respectively]). One replicate plate from each group was set aside and given unlabeled TSM media to act as unlabeled control samples. Untreated and irradiated cells (4Gy) were incubated at 37°C for 3hrs after RT at which point metabolites were extracted.

LC/MS Analysis was performed on an Agilent system consisting of an Infinity Lab II UPLC with a 10-port valve coupled with a 6545 QToF mass spectrometer (Agilent Technologies) using a JetStream ESI source in negative mode. Source parameters: Gas Temp: 250 °C, Gas Flow: 13 L/min, Nebulizer: 35 psi, Sheath Gas Temp: 325 °C, Sheath Gas Flow: 12 L/min, Capillary: 3500 V, Nozzle Voltage: 1500 V.

Chromatographic separation was performed on an Agilent ZORBAX RRHD Extend 80Å C18, 2.1 × 150 mm, 1.8 µm column with an Agilent ZORBAX SB-C8, 2.1 mm × 30 mm, 3.5 µm guard column. The column temperature was 35 °C. Mobile phase A consisted of 97:3 water/ methanol and mobile phase B was 100% methanol; both A and B contained tributylamine and glacial acetic acid at concentrations of 10mM and 15mM, respectively. The column was backflushed with mobile phase C (100% acetonitrile, no additives) between injections for column cleaning.

The LC gradient was as follows: 0-2.5 min, 0% B; 2.5–7.5 min, linear ramp to 20% B min, 7.5–13 min, linear ramp to 45% B; 13–21 min linear ramp to 99% B and held at 99% B until 25 min. At 25 minutes, the 10-port valve was switched to reverse flow (back-flush) through the column, and the solvent composition changed to 95% C and held there for 3 min. From 28 to 28.5 min, the flow rate was ramped to 0.8 mL/min, held until 32.5 min, then reduced to 0.6mL/min. From 32.5 to 33.25 the solvent was ramped from 99–0% C while flow was simultaneously ramped down from 0.6-0.4mL/min and held until 39.9 min., at which point flow rate was returned to starting conditions at 0.25mL/min. The 10-port valve was returned to restore forward flow through the column at 40 min. An isocratic pump was used to introduce reference mass solution through the reference nebulizer for dynamic mass correction. Total run time was 30 min. The injection volume was 5µL. Data was analyzed using MassHunter ProFinder 8.0 software (Agilent Technologies).

Tumor expression data

mRNA-seq Z-score expression and patient survival data from Mackay et al. (2017) was obtained using PedCBioPortal (Children's Hospital of Philadelphia Research Initiative)(2, 30, 31). Data was filtered for patients who had confirmed WT Histone H3 or H3K27M mutant (*H3F3A* or *HIST1H3B*) and the Z-score for each gene of interest was extracted and sorted based on mutational status. Statistical analyses were performed using a two-tailed t-test in GraphPad Prism 9.0.

Long-term neurosphere assay and live cell imaging

H3K27M cells (3x10^5-4x10^5) were cultured in 6-well dishes for 48hrs until they formed small spheres which were then treated with mycophenolic acid (MPA) for 6hrs prior to irradiation in the previously described apparatus. Approximately 18hrs later, spheres were dissociated and replated at low density (500 cells/well) in 96-well plates. Plates were incubated for 5–10 days in a BioSpa incubator (Agilent Technologies) and imaged every 24hrs in a Cytation 5 plate reader with the 4x objective. Gen5 software (Agilent Technologies) was used to analyze the data. A 2D area threshold of 2600um^2 was used to pick spheres, approximating the 50-colony threshold used in standard clonogenic survival assays. End-point sphere numbers were used to calculate the surviving fraction of cells. The Dmid of the 0μM MPA control was divided by the Dmid of the MPA-treated groups to calculate the Enhancement Ratio (ER) to display changes in RT efficacy.

Stereotactic orthotopic implantation

Rag1-KO C57BL/6 mice were anesthetized and provided carprofen analgesic before removing the scalp fur and sterilizing the incision site. An incision was made along the midline of the scalp and a small hole in the skull was made using an electric burr hole drill or handheld drill bit at coordinates 2-3mm lateral, 0.5-1mm rostral or caudal (depending on the injection rig used) from the bregma. Approximately 1.5x10^5-2.0x10^5 cells (~ 5.0x10^4 cells/μL) in a volume of 3μL were implanted in the cortex at depth of approximately 2.5mm using 10μL Hamilton syringes. After injections, wounds were sutured and were given triple antibiotic ointment. Atipamezole was given reverse the anesthetic in heated cages. Mice were given diet gel supplement and monitored for 10 days, including a second dose of carprofen the day following the surgery. For some experiments, a PhD Ultra multi-syringe pump (Harvard Apparatus) was utilized to facilitate simultaneous implantation of up to 8 mice at once. A minimum of 6 mice were used per treatment group in subsequent *in vivo* experiments.

Bioluminescent imaging (BLI) and mouse treatment

Mice were administered sterile-filtered 30mg/mL luciferin solution (Syd Laboratories) via IP injection. Ten minutes post-injection, BLI signal was measured using an IVIS Spectrum imaging station and Luminescent Flux Values were obtained for each tumor. BLI flux values were used to randomize mice into four treatment groups (10 mice/group) based on BLI flux average signal. BLI was repeated 1-2x weekly during efficacy studies. Treatment groups included: Vehicle Control (0.5% w/v methylcellulose, 0.1% Tween-80 in ddH2O, mycophenolate mofetil (MMF) alone, RT alone, and MMF + RT. MMF (150mg/kg)

was administered by oral gavage for 11 consecutive days starting between 13–18 days post-implantation. Mice were sedated using 2.5% isoflurane and RT was administered in 2Gy fractions on days 2, 4–5, 8–9, and 11 of MMF treatment using an Orthovoltage irradiator. Mice were euthanized upon development of neurological symptoms and survival data was analyzed using the Kaplan-Meier method using GraphPad Prism 9.0.

Results

The H3K27M mutation confers global changes to cellular metabolism.

Altered cellular metabolism is a hallmark of cancer(32). To begin to understand how the H3K27M mutation alters metabolism and facilitates treatment resistance, we quantified how metabolite levels differed between normal brain and DMG-H3K27M xenograft tumor tissue. Using fluorescence-guided microdissection, we separated GFP and luciferase-expressing DIPGXIII (DIPGXIII-GFP/LUC) orthotopic tumors from surrounding normal brain and quantified their metabolites. The brain-specific metabolite N-acetylaspartate was higher in cortex compared to DMG tumors, indicating that our fluorescent-based separation was successful (Fig S1A). Numerous other metabolites including dGTP/ATP, citrate/isocitrate, and UDPglcNAC were elevated in DMG while adenine, ureidosuccinate, and aspartate were lower indicating that DMG tumor tissue possesses a distinct metabolome compared to normal brain (Fig. 1A). To understand the biology of these dysregulated metabolites, we performed metabolic pathway enrichment analysis and found enrichment of pyrimidine and methionine metabolism in DMG-H3K27M tumors (blue bars), consistent with recent reports of the importance of these pathways in H3K27M tumors, as well as purine metabolism (Fig. 1B)(25, 26, 29).

Some of these metabolic alterations might be caused specifically by the H3K27M mutation(24) while others might be related to alternative mutations or oncogenic transformation in general. To understand how the H3K27M mutation specifically affected metabolism, we used isogenic patient-derived DMG-H3K27M cell line pairs (DIPGXIII and BT245) in which the H3K27M mutation has been removed from the parental cell line using CRISPR/Cas9 (DIPGXIII-KO and BT245-KO)(20). We confirmed the presence of the mutation in parental cells and the corresponding lack of H3K27me3 (Fig S1B). We quantified metabolites in these isogenic pairs using LC/MS and found that H3K27M-expressing cells have an altered metabolome compared to H3K27M-KO counterparts (Fig. 1B, S2, and Supplemental Table 1). These findings are consistent with prior studies and confirm that the oncohistone plays an active role in altering DMG metabolism(24).

RT induces changes in purine metabolism in H3K27M cells.

We hypothesized that the H3K27M mutation influences the metabolic response to RT, thereby conferring RT resistance(33–35). Using the H3K27M-isogenic models, we performed steady-state metabolomics on untreated and RT-treated cells two hours after RT to capture early shifts in cellular metabolism that might mediate RT resistance (Fig. 1D-E). We identified numerous metabolites that changed following RT in either the H3K27M or H3K27M-KO cells (Fig. 1D-E and Supplemental Table 2). Metabolites like glutamine

in the DIPGXIII cells and aspartate in the BT245 model had similar responses to RT in both H3K27M and H3K27M-KO cells (Fig S3A-B). Other metabolites like xanthine in the DIPGXIII model and dGDP/ADP in the BT245 model had responses to RT that varied depending on the presence of the H3K27M mutation (Fig S3C-D, Supplemental Table 2).

To better understand which metabolic changes were H3K27M-specific, we calculated the differences in fold-change (FC) following RT between H3K27M and H3K27M-KO cell lines for each metabolite (Fig. 1D-E and Supplemental Table 2). We noticed that numerous purine species including xanthine, hypoxanthine, guanine, AMP, and ADP/dGDP responded differently to RT in H3K27M mutant cells compared to KO controls (Fig. 1D-E, Supplemental Table 2). Metabolite set enrichment analysis of the top 25 metabolites highlighted purine metabolism in both H3K27M-isogenic cell line pairs (Fig. 1F-G, H). Other purine metabolism-related pathways found included the pentose phosphate pathway (DIPGXIII) (Fig. 1F) that creates the ribose-5-phosphate sugars needed for nucleotides, and glycine/serine/threonine metabolism (BT245) that generates metabolites needed for purine ring construction (Fig. 1G). We reanalyzed DIPGXIII-GFP/LUC tumor data to focus on purine species and found that tumor tissue has an inverse purine metabolic phenotype to that of the normal tissue (Fig. 1I). Interestingly, our group has shown that purine metabolism mediates treatment resistance in adult glioblastoma (GBM), another form of astrocytoma(16). Together, these observations suggest that purine metabolism changes following RT in an H3K27M-specific fashion.

Purine metabolic flux and enzyme expression are influenced by the H3K27M mutation.

We and others have found that purine species, especially guanylates, contribute to treatment resistance in brain tumors(16, 36). We reasoned that targeting purine synthesis could increase RT efficacy in DMG-H3K27M. Purine nucleotides are produced through either the *de novo* or the salvage synthesis pathways (Fig. 2A). To determine which of these pathways DMG-H3K27M tumors may rely on, we performed stable isotope tracing to measure their baseline flux. This technique utilizes nutrients carrying one or more nonradioactive atoms that are heavier than the naturally occurring form, allowing for their detection by mass spectrometry. Heavy isotope labeling patterns in metabolites formed from the tracer molecule then allows us to track how cells change their metabolic fluxes in response to RT. We tracked *de novo* synthesis (DNS) using ^{15}N-glutamine as it is critical for the formation of newly synthesized purine rings (Fig S4B). Purine salvage was measured using 2D-Hpx that is converted into the common purine precursor, IMP, which can then be converted into GMP or AMP (Fig S4A). Here, we observed that DIPGXIII H3K27M-expressing cells have a significantly higher ratio of ^{15}N-glutamine:2D-Hpx labeling of GMP than do H3K27M-KO cells, indicating that H3K27M cells prefer DNS to create GMP (Fig. 2B). This is further evidenced by higher ^{15}N-glutamine labeling (Fig S4C) and lower 2D-Hpx labeling (Fig S4E) and of GMP in H3K27M cells than in H3K27M-KO cells. There was no H3K27M-specific preference for DNS-derived AMP (Fig. 2C, S4D and F).

Given the H3K27M-specific differences in GMP synthesis, we assessed the expression of the rate limiting enzymes in both *de novo* guanylate synthesis (IMPDH1 and IMPDH2) and guanylate salvage (HGPRT).

Using publicly available RNAseq data from patients bearing pediatric high-grade gliomas (pHGG)(2), we found that H3K27M pHGG tumors expressed less *HPRT1*, which encodes the rate-limiting guanylate salvage enzyme HGPRT (Fig. 1D). At the protein level, we observed increased total expression of IMPDH1 protein (Fig. 2E) and decreased total expression of HGPRT (Fig. 2F) in H3K27M cells compared to H3K27M-KO counterparts. We found no difference in the expression of *IMPDH1* or *IMPDH2* between H3WT or H3K27M pHGG tumors (Fig S5A-B). We also did not observe a difference in the expression of *GMPS*, the gene-encoding the enzyme downstream of *IMPDH1/2* (Fig S5C).

Together, these results suggest that H3K27M cells inactivate guanylate salvage due to decreased expression of HGPRT and have increased reliance on *de novo* guanylate synthesis that is facilitated by increased IMPDH protein expression (Fig. 3A). Consistent with our tracing results, we did not observe similar patterns in the enzymes used to synthesize adenylates or in those used in the upstream steps of DNS (Fig S5D-F).

De novo guanylate synthesis inhibition increases RT efficacy in H3K27M models.

Increased reliance on *de novo* guanylate synthesis in H3K27M expressing cells suggests that inhibition of this pathway may have utility as monotherapy(37) or in combination with RT (Fig. 3A). Inhibition of *de novo* guanylate synthesis using the IMPDH inhibitor mycophenolic acid (MPA) radiosensitizes adult GBM brain tumors and is being evaluated in a Phase 0/1 clinical trial (NCT04477200) in human GBM patients(16, 38). To explore a similar combination strategy in H3K27M cells, we treated DIPGXIII and BT245 patient-derived H3K27M-expressing cells with 0-10uM MPA in combination with increasing doses of RT (0-6Gy) to determine its effect on radiosensitivity. By measuring neurosphere formation over time, we observed dose-dependent decreases in the surviving fraction of DIPGXIII and BT245 neurospheres following RT which was augmented upon addition of MPA at either concentration (1μM and 10μM), leading to increased RT enhancement ratios (DIPGXIII: 1.45 and 1.78, BT245: 1.33 and 1.33) (Fig. 3B-C). This can be observed visually where we see that combined RT and MPA reduces neurosphere size and number in both of our H3K27M-expressing models, even at a low dosage of radiation (Fig. 3D, S6). Interestingly, we and others have observed single agent efficacy of MPA in DMG-H3K27M cells where we see reduced sphere size and number with MPA alone (Fig. 3D, S6). This suggests that DMG-H3K27M cells were more dependent on DNS at baseline, consistent with our isotope tracing studies and with previous reports(39). Taken together, these results show that IMPDH inhibition might help overcome RT resistance in H3K27M-expressing cells.

With these promising *in vitro* results, we next wanted to test the *in vivo* efficacy of RT in combination with IMPDH inhibition in H3K27M expressing tumors. Previous work from our group and others has shown that mycophenolate mofetil (MMF), the pro-drug of MPA, has efficacy in intracranial adult GBM models(16) and we sought to employ a similar strategy here. DIPGXIII-GFP/LUC cells were orthotopically implanted into the cortex and monitored by bioluminescent imaging (BLI). Once tumors were detectable, mice were randomized and treated with RT alone, MMF alone, combined RT and MMF, or vehicle control (Fig. 4A). Mouse weight was largely unaffected by the treatment course (Fig S7). Unlike our *in vitro*

experiments, MMF alone had little effect on tumor size measured by BLI (Fig. 4B). Both RT and MMF + RT decreased tumor bioluminescence, but in both groups, tumors eventually regrew, and we did not observe marked difference between the two groups (Fig. 4B-C). MMF alone had no effect on median survival versus vehicle controls (27d vs 26d, respectively, $p = 0.6$). RT alone increased mouse survival over vehicle control (31.5d), but not in a statistically significant manner. Combination MMF + RT significantly extended survival over vehicle controls (38d vs 26d, $p = 0.006$), but did not cure tumors (Fig. 4D). These findings suggest that while combination MMF + RT treatment extends survival, there may be resistance mechanisms employed by DMG-H3K27M tumors to evade MMF + RT treatment.

H3K27M cells upregulate purine salvage in response to RT.

We reasoned that DMG-H3K27M tumors might upregulate purine metabolism in response to RT and limit the efficacy of MMF *in vivo*. We employed stable isotope tracing to measure the activity of both *de novo* and salvage purine synthesis following RT (Fig. 5, S8). We showed previously that without RT, H3K27M cells converted more glutamine-derived ^{15}N into GMP but not AMP, than did H3K27M-KO cells (Fig. 2B, S4E-F). RT increased ^{15}N incorporation into GMP in H3K27M-KO cells, but H3K27M cells showed no change (Fig. 5A). We also observe decreased ^{15}N-labeled AMP in both H3K27M and H3K27M-KO cells, though this effect is greater in H3K27M-KO cells (Fig S8A). These findings suggest that H3K27M cells do not increase DNS following RT.

Previously we found that H3K27M cells converted less hypoxanthine into GMP than did H3K27M-KO cells at baseline, which suggested that the H3K27M mutation slows guanylate salvage (Figs. 2B, 3A). Unexpectedly, both H3K27M cells and H3K27M-KO cells *increased* hypoxanthine salvage into GMP post-RT (Fig. 5B). This leads to a roughly sixty percent reduction in ratio of Gln:Hpx incorporation into GMP, highlighting increased reliance on salvage synthesis after RT in H3K27M cells (Fig. 5C). There was no change in hypoxanthine-derived AMP in either H3K27M or H3K27M-KO cells (Fig S8B). The ability for H3K27M cells to increase guanylate salvage following RT could account for their resistance to MMF + RT treatment.

To understand how H3K27M cells can upregulate purine salvage but not DNS following RT, we examined the expression of the rate limiting enzymes in these pathways. Consistent with an inability to upregulate DNS, H3K27M cells did not show increased IMPDH1 protein expression following RT (Fig. 5D). However, RT increased HGPRT expression in H3K27M-expressing DIPGXIII cells (Fig. 5E). Thus, while H3K27M mutant cells appear to rely on MPA-sensitive DNS in the unperturbed state, they upregulate MPA-resistant purine salvage synthesis following RT, which may mediate resistance to DNS inhibitors like MMF *in vivo* (Fig. 5F).

HPRT1 loss leads to extended survival in mice bearing DMG-H3K27M xenografts.

HGPRT can salvage both hypoxanthine and guanine (Fig. 3A). Salvaged hypoxanthine is converted to IMP whose conversion into GMP is blocked by MPA/MMF (Fig. 6A). Salvaged guanine, by contrast, directly forms GMP and bypasses IMPDH1 inhibition. Thus, upregulation of guanine salvage would

cause MMF resistance while upregulation of hypoxanthine salvage would not, though both could be mediated by increased HGPRT expression. Our initial neurosphere assays (Fig. 3) were performed in TSM media where hypoxanthine is the dominant available purine base(40). However, the mouse tumor microenvironment is vastly different than the cell culture dish regarding metabolite availability. To determine which bases were available for guanylate salvage in DMG-H3K27M tumors, we analyzed both guanine and hypoxanthine levels in orthotopic DIPGXIII-GFP/LUC tumors and contralateral cortex. While DIPGXIII-GFP/LUC tumors and normal brain contained roughly the same abundance of hypoxanthine, tumor tissue possessed a 34-fold higher abundance of guanine (Fig. 6B). High intratumoral guanine coupled with increased salvage activity following RT (Figs. 5B) and RT-induced increases in HGPRT expression (Fig. 5D) suggest that HGPRT-mediated salvage of guanine can bypass IMPDH1 inhibition in H3K27M cells, leading to continued RT resistance (Fig. 6A) despite MMF treatment.

We then wanted to determine if HGPRT inhibition could increase RT efficacy in DMG-H3K27M xenograft tumors. No blood-brain barrier (BBB)-penetrant HGPRT inhibitors currently exist, so we utilized a pooled shRNA to knockdown *HPRT1* expression in DIPGXIII-GFP/LUC cells (DIPGXIII-GFP/LUC-shHPRT1) (Fig. 6C). These cells were then implanted into the cortices of Rag1-KO mice. Tumor-bearing mice were RT-treated as previously described (Fig. 4A). Mouse weight was largely unaffected by the treatment regimen (Fig. S8). RT alone greatly reduced BLI signal in mice bearing DIPGXIII-GFP/LUC-shHPRT1 tumors (Fig. 6D). Median survival in DIPGXIII-GFP/LUC-shHPRT1 tumors was similar to vehicle control mice in our first experiment (33d vs 26d), suggesting that purine salvage is dispensable for initial tumor growth (Fig. 4D and 6E). However, irradiation of HGPRT-deficient tumors significantly extended survival (> 75d) and led to multiple complete responses (Fig. 6E-F). Lastly, using publicly available patient tumor data, patients bearing H3K27M tumors had an inverse correlation between median survival and *HPRT1* expression (Fig. 6G)(2). Together, these findings indicate that purine salvage through HGPRT may mediate RT resistance in DMG-H3K27M.

Discussion

In this study, we have defined new metabolic strategies to overcome treatment resistance in devastating DMG-H3K27M tumors. Using steady-state and stable isotope tracing metabolomics in patient-derived H3K27M-isogenic cell lines, we found that H3K27M cells preferentially rely on the DNS of guanylates. This reliance is likely due to low HGPRT and high IMPDH1 expression in H3K27M cells. Inhibiting DNS of guanylates potentiated the effects of RT on H3K27M models *in vitro* and *in vivo* but did not cure tumors. Intriguingly, H3K27M cells upregulated guanylate salvage in response to RT, and DMG-H3K27M xenografts had abundant intratumoral guanine. This suggested that RT-induced guanylate salvage might be an adaptive mechanism of RT resistance. Consistent with this model, inhibition of guanylate salvage in DMG-H3K27M tumors overcame RT resistance and led to complete responses in several mice. Together, our findings suggest that DMG-H3K27M tumors rely on both *de novo* and salvage guanylate synthesis, with salvage preferentially contributing to radiation resistance.

Our findings add to the growing body of work showing that altered metabolism is a targetable vulnerability in DMG. These tumors cells preferentially rely on *de novo* pyrimidine synthesis and methionine consumption(25, 26). Like others(39), we have found that DMG-H3K27M tumors also rely on *de novo* guanylate synthesis for survival. However, none of these seminal findings have considered how H3K27M-mediated metabolic changes are related to RT resistance. Here, we unexpectedly discovered that activation of guanylate salvage may be an adaptive mechanism to resist RT. Thus, our work suggests that while strategies targeting methionine, pyrimidine, or *de novo* guanylate synthetic metabolism may be effective as monotherapies, targeting radiation-induced guanylate salvage in combination with RT may be an effective combination strategy to combat DMG-H3K27M tumors.

Our discoveries have important implications for the treatment of DMG-H3K27M patients. Nearly every patient with DMG-H3K27M receives RT, so a drug that selectively overcomes DMG-H3K27M RT resistance by inhibiting guanylate salvage could immediately be tested in combination with RT in patients. In this study, we utilized a genetic approach to inhibit guanylate salvage, which cannot readily be translated to patients. 6-mercaptopurine (6-MP) is an HGPRT inhibitor that is effectively used in acute lymphoblastic leukemia (ALL) patients to maintain remission and has been shown to induce apoptosis in renal cancer cells(41, 42). However, it was shown to have poor BBB penetrance in preclinical studies(41). Acyclic nucleoside phosphonates (ANPs) are being investigated as antimalarial compounds that target *Plasmodium spp.* HGPRT/HG(X)PRT(43). These ANPs were shown to complex with human HGPRT, however it is unknown if they can cross the blood-brain barrier. Preclinical studies to test the pharmacokinetics of molecules like ANPs and drug discovery directed at improving the BBB penetrance of existing inhibitors like 6-MP or development of new molecules could yield new strategies to target RT-induced guanylate salvage in DMG-H3K27M tumors.

These studies present lingering questions that still need to be answered. While we know that RT induces HGPRT expression, we do not know the molecular mechanism behind this upregulation. The rapid change in HGPRT expression (< 3hrs) suggests an epigenetic mechanism that could be related to the underlying H3K27M mutation. Additionally, we do not know if the ratio of DNS to salvage changes further as time progresses. We also do not know the source of the abundant guanine in our xenograft model, which could be due to high turn-over from malignant cells or secretion from non-cancerous cells such as atrocytes(39, 44). Lastly, we do not know if the therapeutic window for inhibiting guanylate salvage will be large enough between normal brain and DMG-H3K27M tissue to improve treatment efficacy. The normal brain salvages purines and HGPRT loss underlies Lesch-Nyan disease, though it is possible that temporary inhibition of HGPRT in normal tissues may be tolerated(45).

Conclusions

Together, our studies suggest that multiple routes of purine synthesis are important for DMG growth. Combining *de novo* purine synthesis inhibition with RT, an approach that we are utilizing clinically for adult patients with GBM(38), may therefore be less promising in DMG. Further preclinical study is needed

to determine if combining small molecule inhibition of purine salvage with radiation can improve RT efficacy and be translated to clinical trials to improve DMG-H3K27M patient outcomes.

Abbreviations

DMG: Diffuse midline glioma

DIPG: Diffuse intrinsic pontine glioma

H3K27M: Histone H3, K27M mutant

RT: Radiation therapy

HGPRT: Hypoxanthine guanine phosphoribosyl transferase

TSM: Tumor stem media

GFP/LUC: Green fluorescent protein/Luciferase

IMPDH: Inosine monophosphate dehydrogenase

LC/MS: Liquid chromatography/Mass spectrometry

2D-Hpx: 2,8-deuterium hypoxanthine

MPA: Mycophenolic acid

ER: Enhancement ratio

BLI: Bioluminescent imaging

MMF: Mycophenolate mofetil

GBM: Glioblastoma

DNS: *De novo* synthesis

BBB: Blood-brain barrier

NIH: National Institute of Health

NCI: National Cancer Institute

NINDS: National Institute of Neurological Disease and Stroke

Declarations

Acknowledgments

We would like to thank the University of Michigan Metabolomics Core for their assistance in performing stable isotope tracing metabolomics experiments.

Ethics approval and consent to participate

Animal studies were conducted according to the guidelines approved by the Institutional Animal Care and Use Committee (IACUC) at the University of Michigan (approved protocol: PRO00010680). Publicly available, pre-published mRNA-seq Z-score expression and patient survival data from Mackay et al. (2017) was obtained using PedCBioPortal (Children's Hospital of Philadelphia Research Initiative)(2, 30, 31).

Data Availability

Human tumor RNAseq Z score data and patient survival data were obtained from the Institute of Cancer Research (London, UK) using PedcBioPortal (Children's Hospital of Philadelphia Research Initiative, https://pedcbioportal.kidsfirstdrc.org/) where it is currently available(2, 30, 31). All other data supporting the findings of this study can be made available upon request to the authors.

Competing interests

CAL is a member of the Editorial Board of Cancer & Metabolism, and has received consulting fees from Astellas Pharmaceuticals, Odyssey Therapeutics, and T-Knife Therapeutics, and is an inventor on patents pertaining to KRAS-regulated metabolic pathways, redox control pathways in pancreatic cancer, and targeting the GOT1-pathway as a therapeutic approach (US patent 2015126580-A1, 05/07/2015; US patent 20190136238, 05/09/2019; international patent WO2013177426-A2, 04/23/2015). DRW has received consulting fees from Agios Pharmaceuticals and Innocrin Pharmaceuticals and is an inventor on patents pertaining to the treatment of patients with brain tumors (U.S. Provisional Patent Application 63/416,146, U.S. Provisional Patent Application 62/744,342, U.S. Provisional Patent Applicant 62 /724,337).

Funding

ERP was supported by grants from the ChadTough Defeat DIPG Foundation, Alex's Lemonade Stand Foundation, and the Rogel Cancer Center at the University of Michigan. PS was supported by National Institute of Health (NIH)/National Cancer Institute (NCI) grants 5T32CA140044-12 and 5T32CA140044-13. AJS was supported by NIH/NCI F32CA260735. WZ was supported by the University of Michigan Medical School Pandemic Recovery Grant U083054. MAM was supported by NIH R01CA240515 and Alex's Lemonade Stand. MGC was supported by the grants from the NIH/National Institute of Neurological Disorders and Stroke (NINDS) grants R37NS094804, R01NS105556, R01NS122536, R01NS124167, and R21NS123879-01, the Rogel Cancer Center, the Department of Neurosurgery at the University of Michigan, The Pediatric Brain Tumor Foundation, Leah's Happy Hearts Foundation, Ian's

Friends Foundation, ChadTough Defeat DIPG Foundation, and Smiles for Sophie Forever Foundation. DRW was supported by grants from the Forbes Institute for Cancer Discovery, by NCI grants K08CA234416 and R37CA258346, by NINDS R01NS129123, the Damon Runyon Cancer Research Foundation, the Sontag Foundation, the Ivy Glioblastoma Foundation, Alex's Lemonade Stand Foundation, the Rogel Cancer Center, and the ChadTough Defeat DIPG foundation. Research reported in this publication was supported by the National Cancer Institutes of Health under award number P30CA046592 by the use of the University of Michigan Rogel Comprehensive Cancer Center Experimental Irradiation Shared Resource.

Authors' Contributions

DRW and ERP conceptualized and designed the study. ERP, DRW, and AJS developed the methods used in this study. MGC provided conceptual design for metabolic pathway nomination experiments. NJ provided H3K27M-isogenic models used in this study. MGC, SV, and CK provided technical training and guidance for animal experiments. MAM provided conceptual guidance in the development of irradiation studies. ERP and CH performed and collected data for the experiments. LZ performed steady-state LC/MS studies. CAL supervised technical staff and metabolomics studies. PS and AA performed data preparation and base analysis for steady-state metabolomics studies. AJS, PS, and AA assisted with metabolomics data analysis. KWR, AL, AO, AK, and ZZ assisted in orthotopic implantation surgeries and treatment. AJS, SP, and NK aided with stable isotope tracing experimental design and interpretation. All authors reviewed the manuscript and provided material support for revisions. All authors read and approved the final version of the manuscript.

Consent for Publication

Not applicable

References

1. Louis DN, Perry A, Reifenberger G, von Deimling A, Figarella-Branger D, Cavenee WK, et al. The 2016 World Health Organization Classification of Tumors of the Central Nervous System: a summary. Acta Neuropathologica. 2016;131(6):803-20.
2. Mackay A, Burford A, Carvalho D, Izquierdo E, Fazal-Salom J, Taylor KR, et al. Integrated Molecular Meta-Analysis of 1,000 Pediatric High-Grade and Diffuse Intrinsic Pontine Glioma. Cancer Cell. 2017;32(4):520-37.e5.
3. Lin GL, Wilson KM, Ceribelli M, Stanton BZ, Woo PJ, Kreimer S, et al. Therapeutic strategies for diffuse midline glioma from high-throughput combination drug screening. Sci Transl Med. 2019;11(519).
4. Schwartzentruber J, Korshunov A, Liu X-Y, Jones DTW, Pfaff E, Jacob K, et al. Driver mutations in histone H3.3 and chromatin remodelling genes in paediatric glioblastoma. Nature. 2012;482(7384):226-31.

5. Himes BT, Zhang L, Daniels DJ. Treatment Strategies in Diffuse Midline Gliomas With the H3K27M Mutation: The Role of Convection-Enhanced Delivery in Overcoming Anatomic Challenges. Frontiers in Oncology. 2019;9.
6. Grasso CS, Tang Y, Truffaux N, Berlow NE, Liu L, Debily MA, et al. Functionally defined therapeutic targets in diffuse intrinsic pontine glioma. Nat Med. 2015;21(6):555-9.
7. Liu SJ, Malatesta M, Lien BV, Saha P, Thombare SS, Hong SJ, et al. CRISPRi-based radiation modifier screen identifies long non-coding RNA therapeutic targets in glioma. Genome Biol. 2020;21(1):83.
8. Mandell LR, Kadota R, Freeman C, Douglass EC, Fontanesi J, Cohen ME, et al. There is no role for hyperfractionated radiotherapy in the management of children with newly diagnosed diffuse intrinsic brainstem tumors: results of a Pediatric Oncology Group phase III trial comparing conventional vs. hyperfractionated radiotherapy. Int J Radiat Oncol Biol Phys. 1999;43(5):959-64.
9. Jansen MH, Veldhuijzen van Zanten SE, Sanchez Aliaga E, Heymans MW, Warmuth-Metz M, Hargrave D, et al. Survival prediction model of children with diffuse intrinsic pontine glioma based on clinical and radiological criteria. Neuro Oncol. 2015;17(1):160-6.
10. Gardner SL, Allen JC, Zaky WT, Odia Y, Daghistani D, Khatib Z, et al. ONC201 in previously-irradiated pediatric H3 K27M-mutant glioma. Journal of Clinical Oncology. 2019;37(15_suppl):10046-.
11. Nikolaev A, Fiveash JB, Yang ES. Combined Targeting of Mutant p53 and Jumonji Family Histone Demethylase Augments Therapeutic Efficacy of Radiation in H3K27M DIPG. Int J Mol Sci. 2020;21(2).
12. Pachocki CJ, Hol EM. Current perspectives on diffuse midline glioma and a different role for the immune microenvironment compared to glioblastoma. J Neuroinflammation. 2022;19(1):276.
13. Werbrouck C, Evangelista CCS, Lobón-Iglesias MJ, Barret E, Le Teuff G, Merlevede J, et al. TP53 Pathway Alterations Drive Radioresistance in Diffuse Intrinsic Pontine Gliomas (DIPG). Clin Cancer Res. 2019;25(22):6788-800.
14. Zhou W, Wahl DR. Metabolic Abnormalities in Glioblastoma and Metabolic Strategies to Overcome Treatment Resistance. Cancers. 2019;11(9).
15. Núñez FJ, Mendez FM, Kadiyala P, Alghamri MS, Savelieff MG, Garcia-Fabiani MB, et al. IDH1-R132H acts as a tumor suppressor in glioma via epigenetic up-regulation of the DNA damage response. Sci Transl Med. 2019;11(479).
16. Zhou W, Yao Y, Scott AJ, Wilder-Romans K, Dresser JJ, Werner CK, et al. Purine metabolism regulates DNA repair and therapy resistance in glioblastoma. bioRxiv. 2020:2020.03.26.010140.
17. Guo F, Li J, Du W, Zhang S, O'Connor M, Thomas G, et al. mTOR regulates DNA damage response through NF-κB-mediated FANCD2 pathway in hematopoietic cells. Leukemia. 2013;27(10):2040-6.
18. Bender S, Tang Y, Lindroth AM, Hovestadt V, Jones DTW, Kool M, et al. Reduced H3K27me3 and DNA hypomethylation are major drivers of gene expression in K27M mutant pediatric high-grade gliomas. Cancer Cell. 2013;24(5):660-72.
19. Krug B, De Jay N, Harutyunyan AS, Deshmukh S, Marchione DM, Guilhamon P, et al. Pervasive H3K27 Acetylation Leads to ERV Expression and a Therapeutic Vulnerability in H3K27M Gliomas. Cancer

Cell. 2019;35(5):782-97.e8.
20. Harutyunyan AS, Krug B, Chen H, Papillon-Cavanagh S, Zeinieh M, De Jay N, et al. H3K27M induces defective chromatin spread of PRC2-mediated repressive H3K27me2/me3 and is essential for glioma tumorigenesis. Nature Communications. 2019;10.
21. Harutyunyan AS, Chen H, Lu T, Horth C, Nikbakht H, Krug B, et al. H3K27M in Gliomas Causes a One-Step Decrease in H3K27 Methylation and Reduced Spreading within the Constraints of H3K36 Methylation. Cell Rep. 2020;33(7):108390.
22. Wu G, Diaz AK, Paugh BS, Rankin SL, Ju B, Li Y, et al. The genomic landscape of diffuse intrinsic pontine glioma and pediatric non-brainstem high-grade glioma. Nature Genetics. 2014;46(5):444-50.
23. Larson JD, Kasper LH, Paugh BS, Jin H, Wu G, Kwon CH, et al. Histone H3.3 K27M Accelerates Spontaneous Brainstem Glioma and Drives Restricted Changes in Bivalent Gene Expression. Cancer Cell. 2019;35(1):140-55.e7.
24. Chung C, Sweha SR, Pratt D, Tamrazi B, Panwalkar P, Banda A, et al. Integrated Metabolic and Epigenomic Reprograming by H3K27M Mutations in Diffuse Intrinsic Pontine Gliomas. Cancer Cell. 2020;38(3):334-49.e9.
25. Pal S, Kaplan JP, Nguyen H, Stopka SA, Savani MR, Regan MS, et al. A druggable addiction to de novo pyrimidine biosynthesis in diffuse midline glioma. Cancer Cell. 2022;40(9):957-72.e10.
26. Golbourn BJ, Halbert ME, Halligan K, Varadharajan S, Krug B, Mbah NE, et al. Loss of MAT2A compromises methionine metabolism and represents a vulnerability in H3K27M mutant glioma by modulating the epigenome. Nat Cancer. 2022;3(5):629-48.
27. Tsoli M, Liu J, Franshaw L, Shen H, Cheng C, Jung M, et al. Dual targeting of mitochondrial function and mTOR pathway as a therapeutic strategy for diffuse intrinsic pontine glioma. Oncotarget. 2018;9(7):7541-56.
28. Kerk SA, Lin L, Myers AL, Sutton DJ, Andren A, Sajjakulnukit P, et al. Metabolic requirement for GOT2 in pancreatic cancer depends on environmental context. Elife. 2022;11.
29. Pang Z, Chong J, Zhou G, de Lima Morais DA, Chang L, Barrette M, et al. MetaboAnalyst 5.0: narrowing the gap between raw spectra and functional insights. Nucleic Acids Res. 2021;49(W1):W388-w96.
30. Cerami E, Gao J, Dogrusoz U, Gross BE, Sumer SO, Aksoy BA, et al. The cBio cancer genomics portal: an open platform for exploring multidimensional cancer genomics data. Cancer Discov. 2012;2(5):401-4.
31. Gao J, Aksoy BA, Dogrusoz U, Dresdner G, Gross B, Sumer SO, et al. Integrative analysis of complex cancer genomics and clinical profiles using the cBioPortal. Sci Signal. 2013;6(269):pl1.
32. Hanahan D, Weinberg RA. Hallmarks of cancer: the next generation. Cell. 2011;144(5):646-74.
33. Cruz-Gregorio A, Martínez-Ramírez I, Pedraza-Chaverri J, Lizano M. Reprogramming of Energy Metabolism in Response to Radiotherapy in Head and Neck Squamous Cell Carcinoma. Cancers (Basel). 2019;11(2).

34. Warburg O. On the origin of cancer cells. Science. 1956;123(3191):309-14.
35. Kunkel M, Moergel M, Stockinger M, Jeong JH, Fritz G, Lehr HA, et al. Overexpression of GLUT-1 is associated with resistance to radiotherapy and adverse prognosis in squamous cell carcinoma of the oral cavity. Oral Oncol. 2007;43(8):796-803.
36. Shireman JM, Atashi F, Lee G, Ali ES, Saathoff MR, Park CH, et al. De novo purine biosynthesis is a major driver of chemoresistance in glioblastoma. Brain. 2021;144(4):1230-46.
37. Lulla RR, Saratsis AM, Hashizume R. Mutations in chromatin machinery and pediatric high-grade glioma. Sci Adv. 2016;2(3):e1501354.
38. Umemura Y, Sun Y, Junck L, Leung D, Kim M, Al-Holou W, et al. DDRE-19. PHASE 0/I TRIAL OF MYCOPHENOLATE MOFETIL COMBINED WITH RADIATION TO OVERCOME GLIOBLASTOMA TREATMENT RESISTANCE BY TARGETING DE-NOVO PURINE METABOLISM. Neurooncol Adv. 3: © The Author(s) 2021. Published by Oxford University Press, the Society for Neuro-Oncology and the European Association of Neuro-Oncology.; 2021. p. i10.
39. Zhao G, Newbury P, Ishi Y, Chekalin E, Zeng B, Glicksberg BS, et al. Reversal of cancer gene expression identifies repurposed drugs for diffuse intrinsic pontine glioma. Acta Neuropathol Commun. 2022;10(1):150.
40. Lin GL, Monje M. A Protocol for Rapid Post-mortem Cell Culture of Diffuse Intrinsic Pontine Glioma (DIPG). J Vis Exp. 2017(121).
41. Deguchi Y, Yokoyama Y, Sakamoto T, Hayashi H, Naito T, Yamada S, et al. Brain distribution of 6-mercaptopurine is regulated by the efflux transport system in the blood-brain barrier. Life Sci. 2000;66(7):649-62.
42. Wilde BR, Chakraborty N, Matulionis N, Hernandez S, Ueno D, Gee ME, et al. FH variant pathogenicity promotes purine salvage pathway dependence in kidney cancer. Cancer Discov. 2023.
43. Hocková D, Keough DT, Janeba Z, Wang TH, de Jersey J, Guddat LW. Synthesis of novel N-branched acyclic nucleoside phosphonates as potent and selective inhibitors of human, Plasmodium falciparum and Plasmodium vivax 6-oxopurine phosphoribosyltransferases. J Med Chem. 2012;55(13):6209-23.
44. Bettio LE, Gil-Mohapel J, Rodrigues AL. Guanosine and its role in neuropathologies. Purinergic Signal. 2016;12(3):411-26.
45. Seegmiller JE, Rosenbloom FM, Kelley WN. Enzyme defect associated with a sex-linked human neurological disorder and excessive purine synthesis. Science. 1967;155(3770):1682-4.

Figures

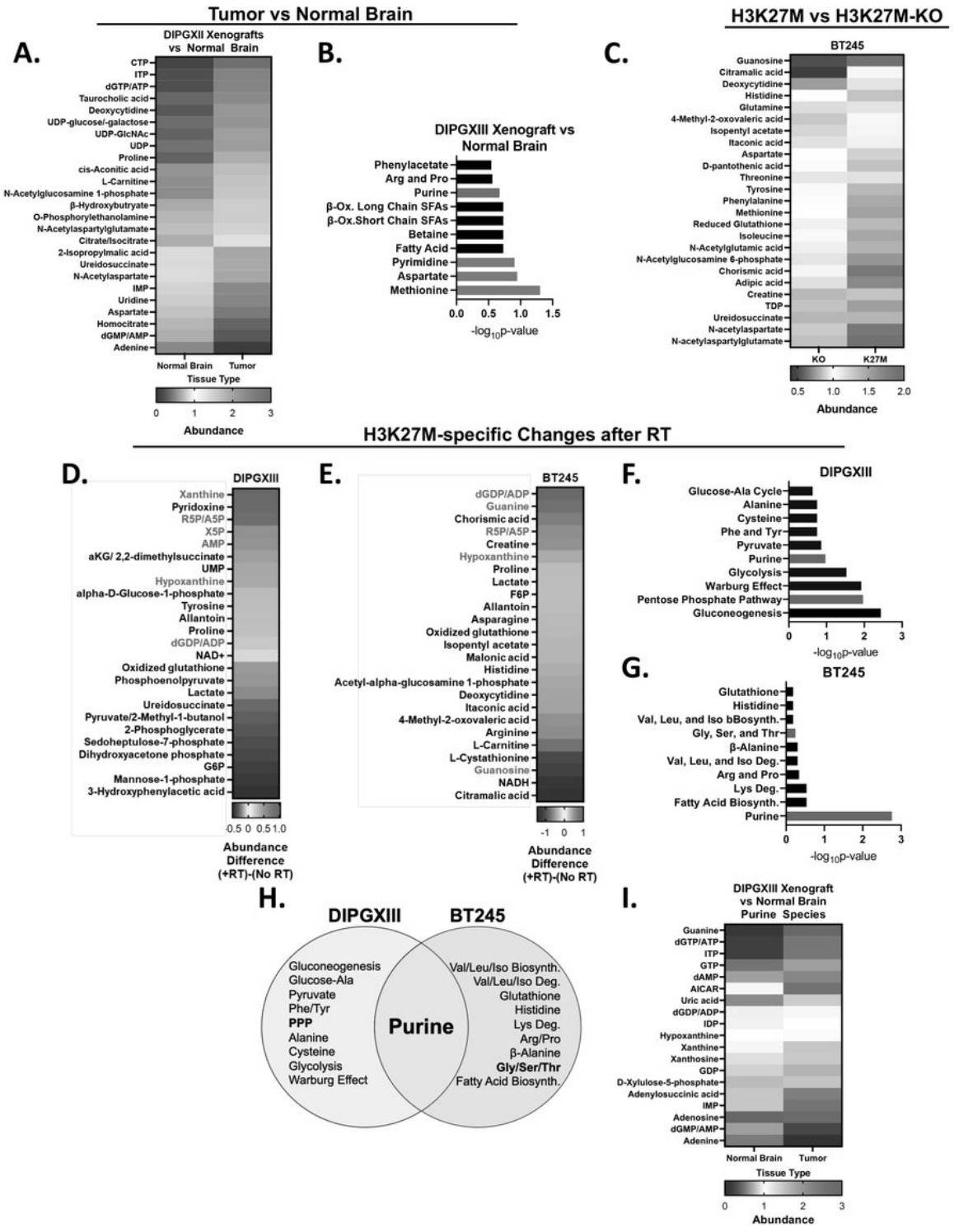

Figure 1

The H3K27M mutation influences metabolic phenotypes and the metabolic response to radiation. *A.)* Untreated intracranial DIPGXIII xenografts and contralateral normal brain issue (n=2 mice/group) were harvested, and their metabolites were collected by methanol extraction and measured using LC/MS. Data are presented as the top 25 significantly different metabolites between Tumor and NB and are ordered by difference in average median centered abundance between K27M and KO cells (K27M-KO). *B.)* Metabolite

set enrichment analysis of all metabolites whose abundance were significantly different between Tumor and normal brain (83 total). Blue bars indicate pathways important for DMG-H3K27M biology as reported in the literature. Red bars indicate pathways important for purine metabolism. *C.)* Metabolites levels in untreated BT245 isogenic cell lines as measured using LC/MS. Data represent the top 25 significantly different metabolites between *H3F3A* KO and K27M cells. Data are ordered by difference in median centered abundance in descending order. Metabolite extractions were performed in triplicate. *D. and E.)* H3K27M isogenic cell lines DIPGXIII *(D.)* and BT245 *(E.)* were treated with or without 4Gy RT and harvested for metabolite quantification 2hrs later. Metabolites meeting the FC threshold were selected. Data represent the top 25 largest absolute post-RT abundance differences between H3K27M and *H3F3A* KO cells in descending order. Red indicates abundances over a post-RT FC value of 0.0. Blue indicates abundances under a post-RT FC value of 0.0. *F. and G.)* Metabolic set enrichment analysis was performed on the metabolite lists for DIPGXIII *(D.)* and BT245 *(E.)* and ordered based on $-\log_{10}$p-value. Red bars indicate pathways important for purine metabolism. *H.)* Venn Diagram depicting the metabolic pathways enriched in RT-treated DMG-H3K27M isogenic cell lines. Bold-faced font indicates metabolic pathways important for purine metabolism and synthesis. *I.)* Purine metabolites from DIPGXIII xenograft tumors and contralateral normal brain from *A.*) were compared and ordered by difference in average median centered abundance between tumor and normal brain.

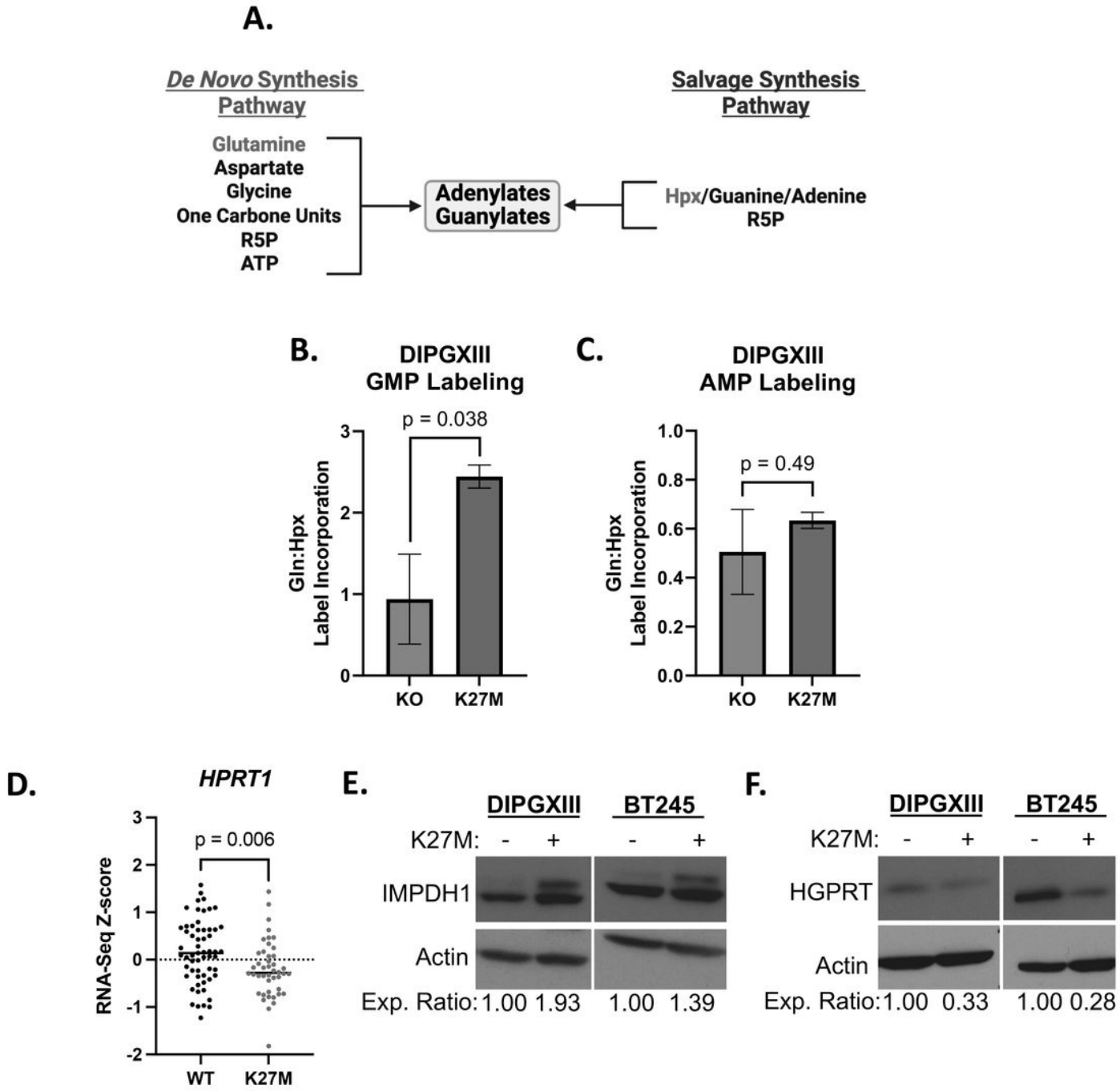

Figure 2

Increased reliance on *de novo* purine synthesis in H3K27M cells. *A.)* Schematic of purine synthetic metabolic pathways showing where the purine *de novo* and salvage pathways converge to form guanylate purines from IMP and free purine bases, respectively. *B.* and *C.)* Ratio of ^{15}N-glutamine:2D-Hpx stable isotope tracer label incorporation into GMP *(B.)* and AMP *(C.)* in untreated DIPGXIII H3K27M-isogenic cell lines. *D.)* Publicly available RNAseq Z-score data for *HPRT1* transcript expression from

pediatric high-grade gliomas (pHGG) was obtained through PedCBioPortal and filtered to include only samples with known H3 mutational status (for both *H3F3A* and *HIST1H3B*) to include all known H3WT (n=59)and combined H3K27M (H3F3A-mut+*HIST1H3B*-mut) samples (n=44) *E.) and F.)* Immunoblots of HGPRT and IMPDH1 *(E.)* and HGPRT *(F.)* expression in DMG-H3K27M isogenic paired cell lines. Densitometric values were calculated using ImageJ software and expression values were normalized to H3K27M-KO cells. Expression ratios are listed below the blot images. Statistical analyses were performed using two-tailed t-tests.

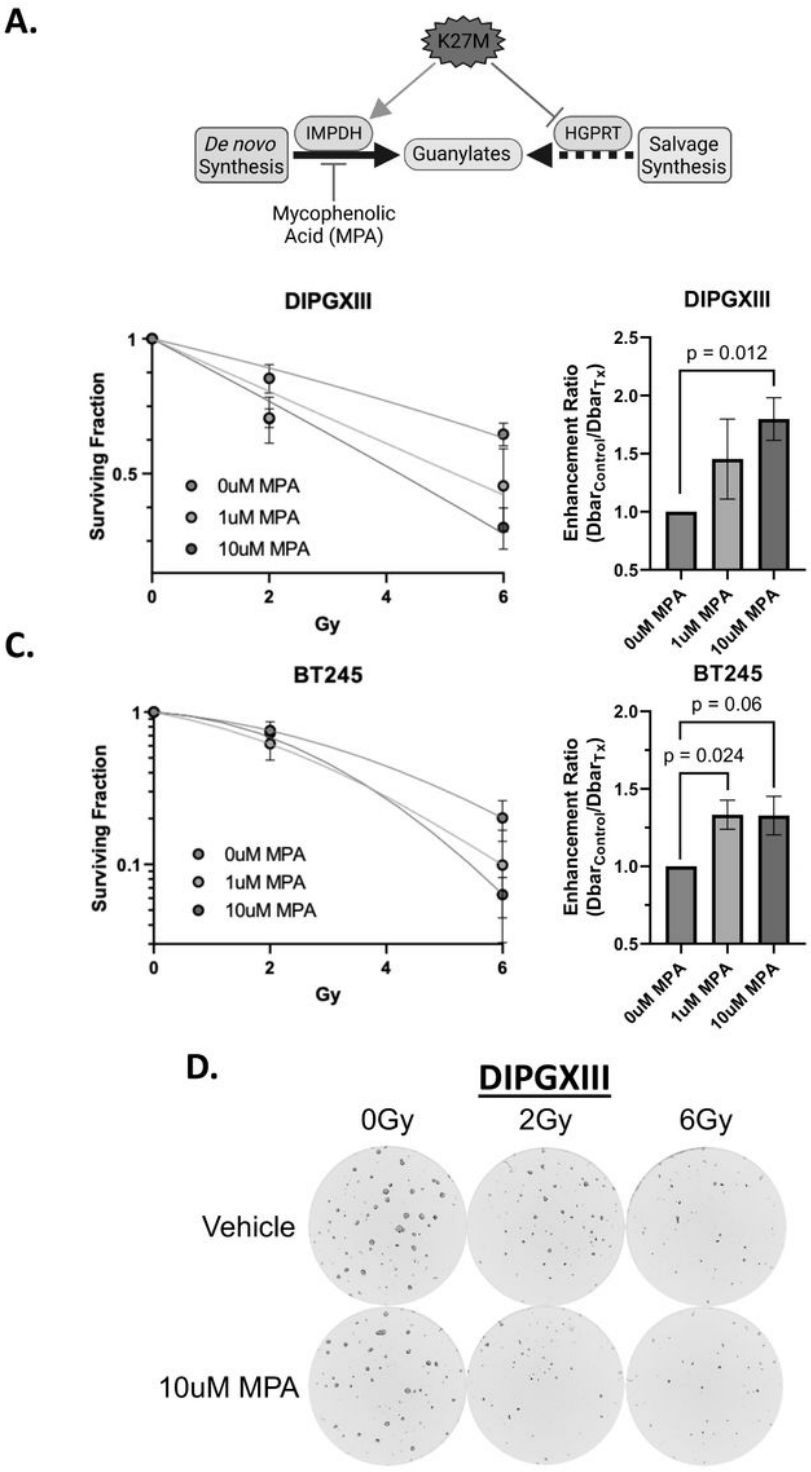

Figure 3

***De novo* purine synthesis inhibition radiosensitizes K27M cells.** *A.)* Schematic depicting the hypothesis that the K27M mutation induces defective guanylate purine salvage through HGPRT suppression, leaving K27M cells vulnerable to *de novo* guanylate synthesis using IMPDH inhibition using MPA. *B. and C.)* Long-term neurosphere growth assays for DIPGXIII *(B.)* and BT245 *(C.)* H3K27M-expressing cell lines treated with increasing doses of RT (0, 2, 6Gy) with or without 1-10mM MPA (*left*) and corresponding enhancement ratio ($Dbar_{control}/Dbar_{Tx}$) for each concentration of MPA (*right*) administered with RT. Each long-term neurosphere assay was performed 3x per cell line. Statistical analyses were performed using two-tailed t-tests. *D.)* Live cell imaging analysis of DIPGXIII neurospheres treated with 0-6Gy +/- 10mM MPA. Images taken 12 days after replating in a 96-well plate. Images acquired using a Cytation 5 plate reader and attached BioSpa incubator (Agilent Technologies).

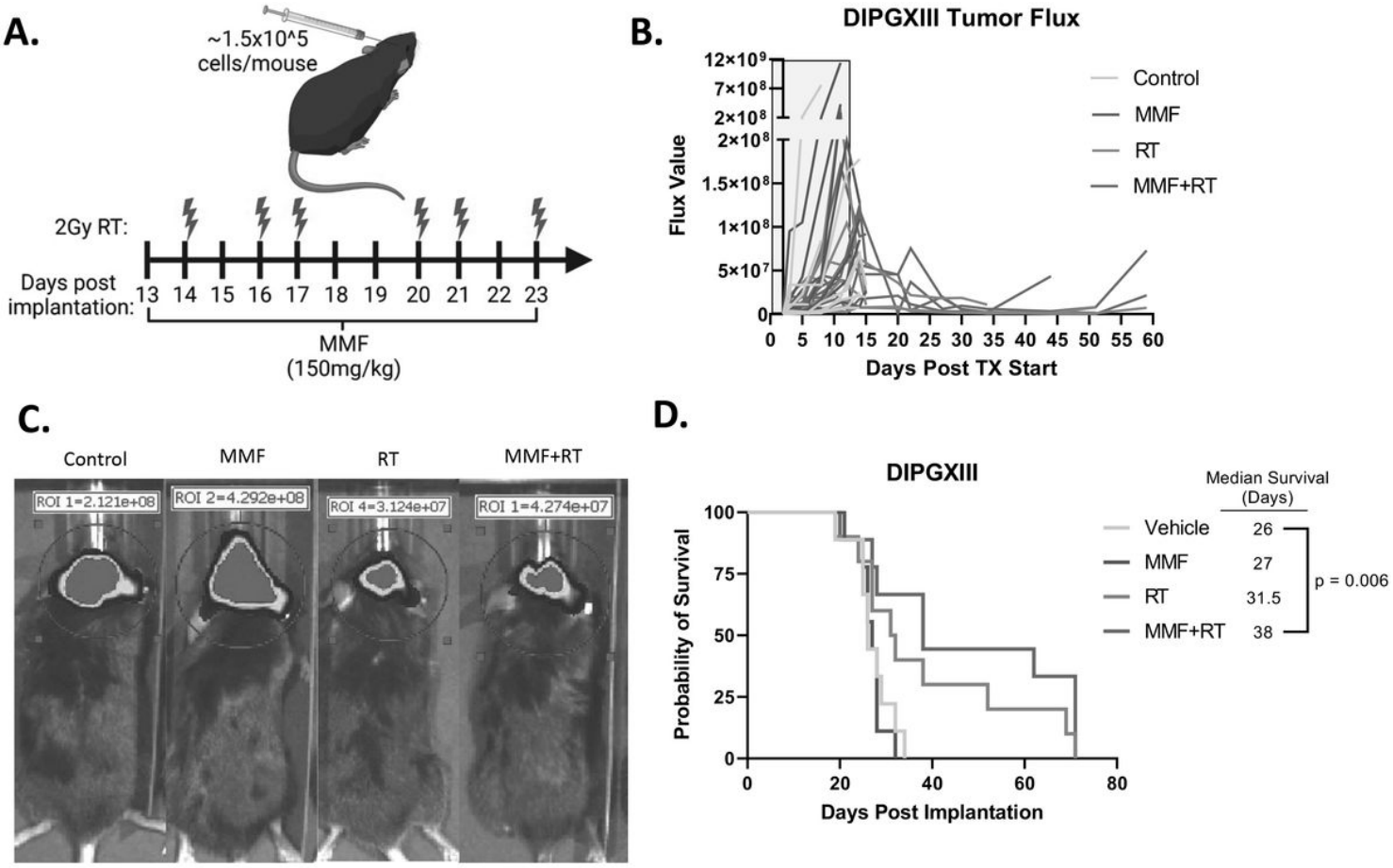

Figure 4

Combination RT and *de novo* purine synthesis inhibition reduces DMG-H3K27M tumor size and extends mouse survival in vivo. *A.)* Schematic of treatment schedule administered to DIPGXIII-bearing Rag1-KO mice. DIPGXIII cells expressing GFP and Luciferase (LUC) (DIPGXIII-GFP/LUC) were orthotopically

implanted into the cortex and mice were administered 150mg/kg MMF for 11 days, with 6 intermittent doses of 2Gy RT (red bolts). *B.)* Spider plot of bioluminescent signal flux values for individual mouse tumors. Blue box indicates the treatment period. *C.)* Representative bioluminescent signal images for one mouse per treatment group 24 days after implantation. *D.)* Kaplan-Meier survival analysis of Rag1-KO mice bearing treated and untreated DIPGXIII-GFP/LUC orthotopic xenograft tumors (n=10 mice/group). Statistical analysis was performed by comparing individual survival curves of individual treatment groups in GraphPad Prism 9.0.

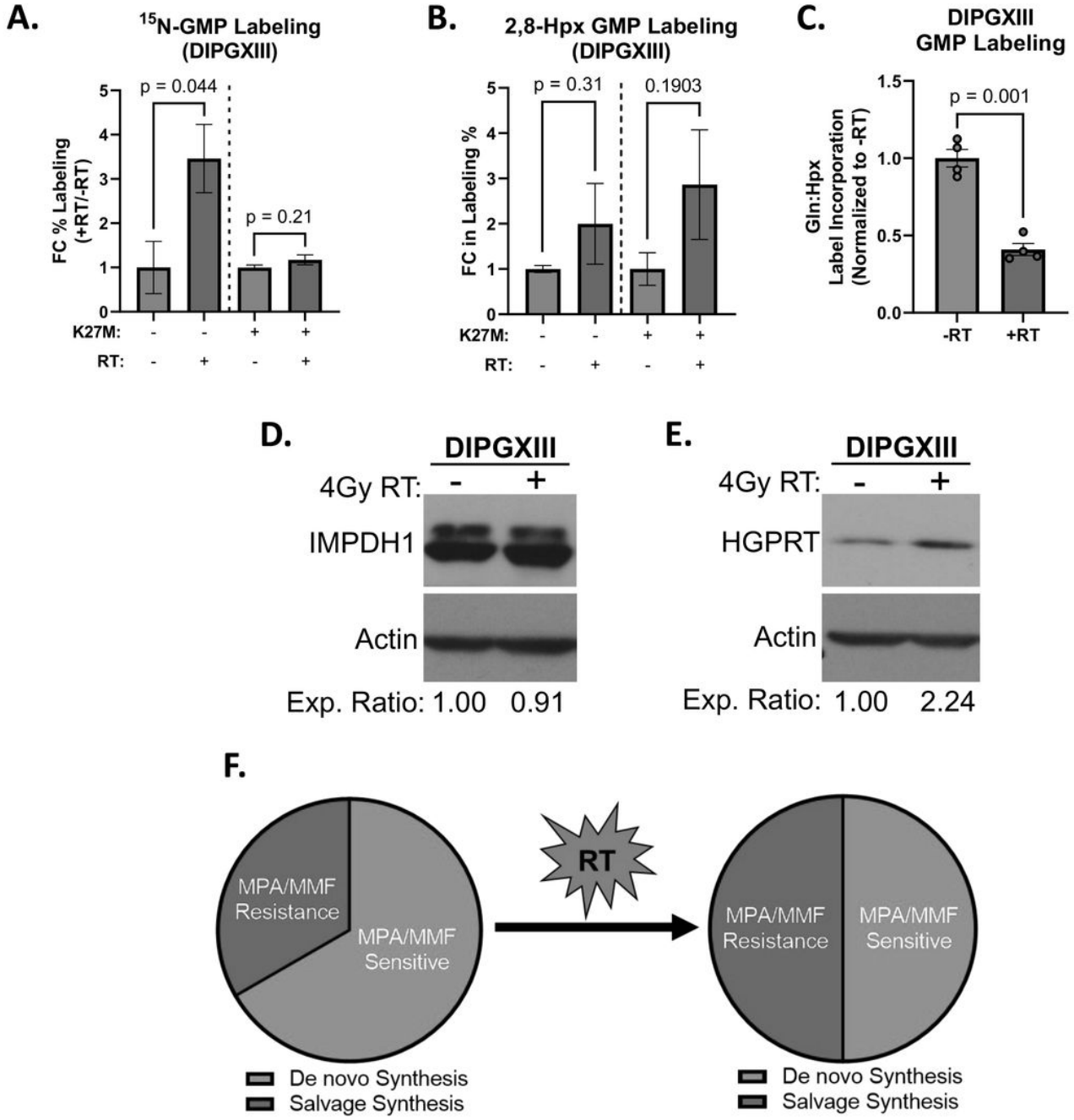

Figure 5

H3K27M-expressing cells increase purine salvage following RT. *A.)* Fold change of the percentage of total GMP in DIPGXIII H3K27M-isogenic cell lines labeled by ^{15}N-glutamine tracer before (gray bars) and 3hrs after 4Gy RT (red bars). Data are normalized to untreated control samples. *B.)* Percent of total GMP in DIPGXIII H3K27M-isogenic cell lines labeled by 2D-Hpx tracer before (gray bars) and 3hrs after 4Gy RT (red bars). Data are normalized to untreated control samples. *C.)* Ratio of Gln:Hpx label incorporation into GMP after 3 hours in DIPGXIII cells that were either untreated or treated with 4Gy RT. Data is normalized to untreated control. *D.)* Immunoblot of IMPDH expression before and after 4Gy RT in DIPGXIII cells. Densitometric analysis was performed using ImageJ software and expression values were normalized to No-RT controls. Values are listed below the blot images. *E.)* Immunoblot of HGPRT expression before and after 4Gy RT in DIPGXIII cells. Densitometric analysis was performed using ImageJ software and expression values were normalized to No-RT controls. Values are listed below the blot images. *F.)* Schematic depicting the RT-induced shift in DNS and salvage flux that leads to a loss of MPA sensitivity. Statistical analyses were performed using two-tailed t-tests in GraphPad Prism 9.0.

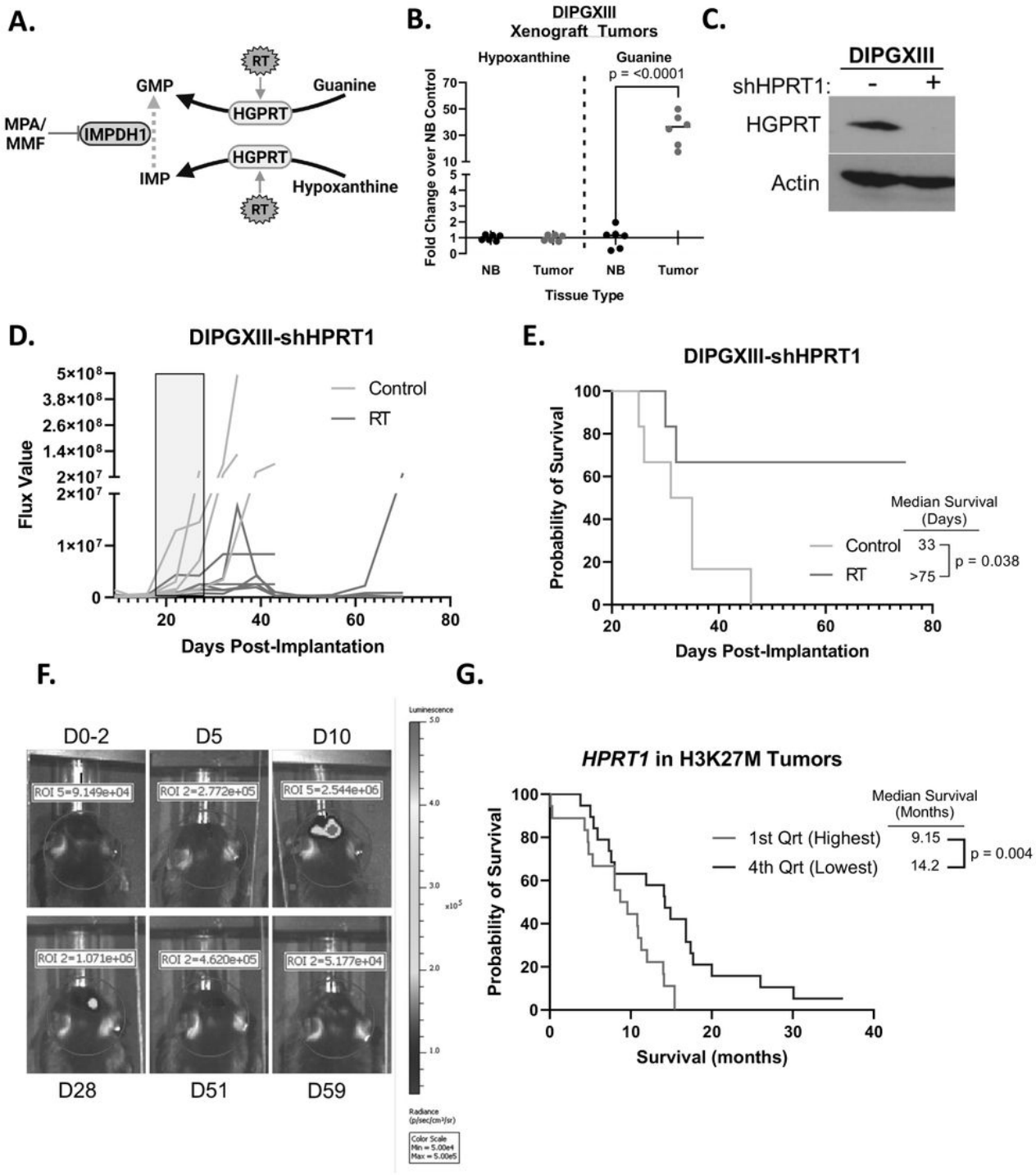

Figure 6

Genetic inhibition of purine salvage in H3K27M-expressing tumors potentiates the effects of RT. *A.)* Schematic showing mechanism of *in vivo* resistance to MMF via increased intratumoral guanine abundance. *B.)* Hypoxanthine and guanine abundances in orthotopic DIPGXIII-GFP/LUC xenograft tumors and contralateral normal brain tissue. Tissues were harvested by GFP fluorescence-guided mechanical resection, and their metabolites collected via methanol extraction before LC/MS. Data is

normalized to normal brain (NB). *C.)* Immunoblot of HGPRT in DIPGXIII-GFP/LUC-shHPRT1 cells transfected with pooled shHPRT1 lentivirus and selected with puromycin. *D.)* Spider plot of bioluminescent signal flux values for individual mouse tumors. Blue box indicates the treatment course. *E.)* Kaplan-Meier survival analysis of Rag1-KO mice bearing DIPGXIII-GFP/LUC-shHPRT1 orthotopic xenograft tumors given vehicle control or RT (n=7 mice/group). Statistical analysis was performed by comparing individual survival curves using GraphPad Prism 9.0 software. *F.)* Bioluminescent imaging of an RT-treated mouse bearing an orthotopic DIPGXIII-GFP/LUC-shHPRT1 xenograft tumor that experienced a complete response following treatment. D# indicates the day at which the image was taken with respect to the end of the treatment regimen. The first image was taken two days prior to the completion of the treatment regimen (D0-2). *G.)* Kaplan-Meier survival analysis of patient H3K27M-expressing tumors based on *HPRT1* expression where the 1st quartile represents the highest *HPRT1* expression, and the 4th quartile represents the lowest *HPRT1* expression.

Supplementary Files

This is a list of supplementary files associated with this preprint. Click to download.

- AdditionalFile1SupplementalFigure1.pdf
- AdditionalFile2SupplementalFigure2.pdf
- AdditionalFile3SupplementalTable1.pdf
- AdditionalFile4SupplementalTable2.pdf
- AdditionalFile5SupplementalFigure3.pdf
- AdditionalFile6SupplementalFigure4.pdf
- AdditionalFile7SupplementalFigure5.pdf
- AdditionalFile8SupplementalFigure6.pdf
- AdditionalFile9SupplementalFigure7.pdf
- AdditionalFile10SupplementalFigure8.pdf
- AdditionalFile11SupplementalFigure9.pdf
- AdditionalFile12SupplementalFiguresTableLegends.docx
- AdditionalFile13AmendmentCompleteBlotImages.pdf